https://ntrs.nasa.gov/search.jsp?R=20120018039 2019-08-30T23:28:22+00:00Z

Turbulent Statistics from Time-Resolved PIV Measurements of a Jet Using Empirical Mode Decomposition

Milo D. Dahl*

NASA Glenn Research Center, Cleveland, OH, 44135, USA

Empirical mode decomposition is an adaptive signal processing method that when applied to a broadband signal, such as that generated by turbulence, acts as a set of band-pass filters. This process was applied to data from time-resolved, particle image velocimetry measurements of subsonic jets prior to computing the second-order, two-point, space-time correlations from which turbulent phase velocities and length and time scales could be determined. The application of this method to large sets of simultaneous time histories is new. In this initial study, the results are relevant to acoustic analogy source models for jet noise prediction. The high frequency portion of the results could provide the turbulent values for subgrid scale models for noise that is missed in large-eddy simulations. The results are also used to infer that the cross-correlations between different components of the decomposed signals at two points in space, neglected in this initial study, are important.

I. Introduction

Computational approaches to predicting jet noise may be categorized as acoustic analogy and numerical methods. The acoustic analogy methods use a rearrangement of the governing equations. The resulting equation contains a linear operator on one side of the equation that reduces to the wave equation for acoustic propagation at large distances from the source region. On the other side of the equation are terms that are significant within a relatively small region and are identified as the equivalent or analogous acoustic sources. The formal solution for the acoustic spectrum in the far field typically involves a convolution integral containing a wave propagator function and a correlation function of turbulence terms in the flow field.[1] Numerical methods based on direct numerical simulation attempt to compute all the scales of turbulence in a flow followed by the computation of the associated radiated noise field. This type of computation requires a large amount of computer resources and time. Using less computer resources, large-eddy simulations compute the relatively larger scales of turbulence in the jet flow field. Consequently, higher frequency noise is missing from the resulting acoustic field spectrum calculations since the computational grid is too large to capture the turbulent noise sources at smaller subgrid scales. Thus, subgrid scale noise models have been proposed following the acoustic analogy approach.[2] Whether the full acoustic spectrum or just the high frequency portion of the acoustic spectrum is to be predicted, these methods require turbulence statistics from flow field measurements. Bodony & Lele,[3] using spatial filtering of a highly resolved, direct numerical simulation of a two-dimensional, low-Reynolds-number shear layer, computed the statistics for both the resolved, large-eddy-simulation-type scales and the unresolved, subgrid scales of turbulence. The parameters for the spatial filter had to be determined prior to its use. In this paper, empirical mode decomposition is used on measured data from jets to filter the data and separate the turbulent scales prior to the computation of turbulent statistics. The decomposition effectively filters the data in a manner that is automatic and signal dependent.

Empirical mode decomposition (EMD) is a recently developed, adaptive signal processing method for any general, non-stationary, and nonlinear signal.[4] The method separates the data signal into a series of basis functions, called intrinsic mode functions, using the data itself. The intrinsic mode functions (IMFs) derived from signal decomposition have been used to distinguish physical phenomena of different frequencies and

*Senior Research Scientist, Senior Member AIAA

wavelengths regardless of the long or short duration of the signal. For example, the method has been applied to study classical nonlinear systems, wind and water wave interactions, ocean waves and tides, tsunami waves, seismic waves, and atmospheric turbulence.[5] The newness of the method and its current issues, such as its limited mathematical foundation and uniqueness,[6] have not slowed its successful application. After a description of the velocity field measurements using time-resolved, particle image velocimetry (TR-PIV) and the jet operating conditions, a description is given of the EMD method as applied in this study. The application of EMD on a large set of simultaneous time histories generated by TR-PIV and subsequently computing two-point, space-time correlations is new.

This paper provides some initial results determined from the second-order, two-point, space-time correlations and spectra computed using the total signals consisting of the flow velocity time histories from TR-PIV and the IMFs of the decomposed signals. Surveys of the axial fluctuating velocity signal and the IMF components of the decomposed signal space-time correlations are given at three reference points near the lipline of two subsonic jets. From the correlations, turbulence phase velocities and integral length and time scales are determined. For the higher speed jet of the two measured jets, the frequency dependent version of these turbulence values are presented and compared to the correlation derived values. It is the highest frequency IMF results for the phase velocities and the length and time scales that may be applicable to subgrid scale noise source modeling. Finally, as a prelude to future work, the importance of the cross-correlation between IMFs is considered.

II. Description of Test Measurements

An extensive set of measured jet noise and flow data has been acquired using the Small Hot Jet Acoustic Rig at the NASA Glenn Research Center.[7] Included in that set is data from time-resolved, particle image velocimetry (TR-PIV). Using this technique, velocity fields were measured in a jet flow at resolutions in both space and time suitable for computing spatial-temporal correlations and spectra. The details of the technique and the methods of data acquisition are found in Wernet[8] and in Bridges & Wernet.[9] Data from jets issuing from a converging nozzle with exit diameter $D = 50.8\,\text{mm}$ operating at exit Mach numbers of 0.51 and 0.98 were used in this paper. The operating conditions for both jets, respectively labelled SP3 and SP7, are shown in Table 1 where T_t/T_∞ is the total temperature ratio relative to ambient conditions, T_s/T_∞ is the static temperature ratio, P_t/P_∞ is the nozzle pressure ratio, M_J is the jet Mach number, U_J/c_∞ is the jet acoustic Mach number, U_J is the jet exit velocity, and c_∞ is the ambient speed of sound.

Case	T_t/T_∞	T_s/T_∞	P_t/P_∞	M_J	U_J/c_∞	U_J(m/s)
SP3	1.00	0.95	1.20	0.51	0.50	172.8
SP7	1.00	0.84	1.85	0.98	0.90	310.0

Table 1. Test conditions for convergent nozzle flow measurements.

As discussed in Wernet,[8] the size of the TR-PIV measurement field depends on the sampling or camera framing rate. The higher the sampling rate, the smaller the field of view becomes. With additional considerations such as the amount of storage space available for the data, the amount of data that can be obtained determines the length of the time histories for the TR-PIV measurements. The jet cases listed in the table were sampled at 25 kHz with a time history length of about 1 second resulting in the maximum Strouhal number for analysis of 3.67 for case SP3 and 2.05 for case SP7 with resolutions in Strouhal number of 0.014 and 0.008, respectively. The measured field was 178.85 mm wide in the axial direction and 5.18 mm wide in the radial direction with a discretization of 70 by 5. The spatial resolutions are $\Delta x/D = 0.0510$ and $\Delta r/D = 0.0255$. Figure 1 shows a representation of the nozzle and the three TR-PIV measurement locations with equal scale in the r/D and x/D direction.

Mean and turbulence quantities computed from the measured TR-PIV data are shown in Figures 2 to 4. The mean axial velocity contours in Figure 2 reflect the wide disparity between the axial and radial dimensions. The negative sign on the radius is maintained by convention with the measurement coordinates, indicating that the measurements were made near the lipline below the centerline of a horizontal jet as shown in Figure 1. Line plots along each of the five radial measurement locations are shown for the normalized mean axial velocity in Figure 3. The lowest mean axial velocities occur along the line $r/D = -0.49$, nearest to the lipline of the jets. Figure 4 shows a similar set of line plots for the normalized axial turbulence

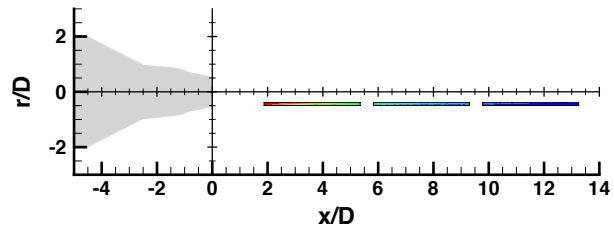

Figure 1. TR-PIV measurement domain size and location relative to the nozzle.

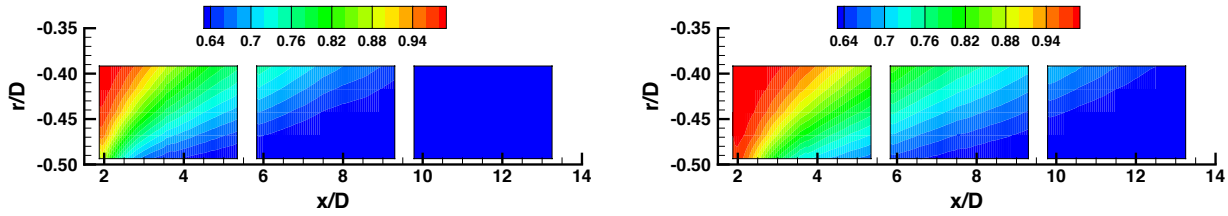

(a) SP3 jet with $M_J = 0.51$, $T_t/T_\infty = 1.00$

(b) SP7 jet with $M_J = 0.98$, $T_t/T_\infty = 1.00$

Figure 2. Mean axial velocity contour plots.

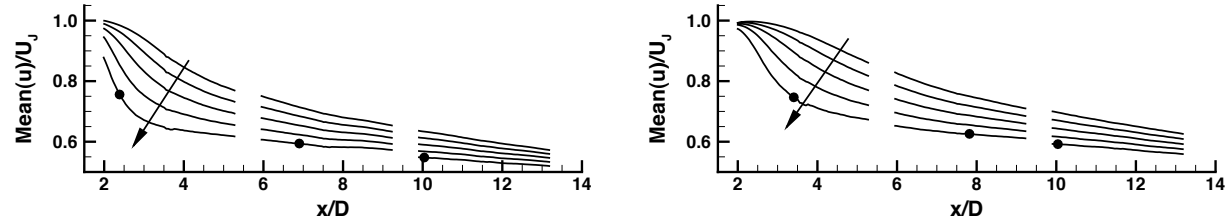

(a) SP3 jet with $M_J = 0.51$, $T_t/T_\infty = 1.00$

(b) SP7 jet with $M_J = 0.98$, $T_t/T_\infty = 1.00$

Figure 3. Mean axial velocities at 5 equidistant radial locations from about $r/D = -0.39$ to -0.49. Arrow points toward velocities at increasing radius. Dot marks reference point conditions.

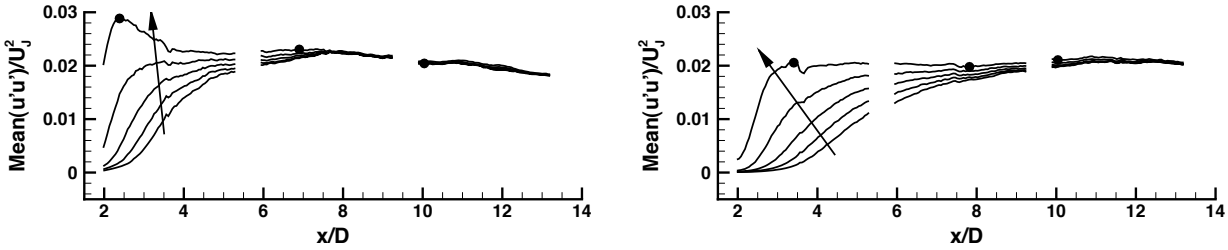

(a) SP3 jet with $M_J = 0.51$, $T_t/T_\infty = 1.00$

(b) SP7 jet with $M_J = 0.98$, $T_t/T_\infty = 1.00$

Figure 4. Axial turbulence intensities at 5 equidistant radial locations from about $r/D = -0.39$ to -0.49. Arrow points toward turbulence intensities at increasing radius. Dot marks reference point conditions.

intensities. Nearer to the nozzle exit the higher intensities occur near the lipline. These results are based on non-overlapping TR-PIV measurement locations. The middle location between about x/D of 6 and 10 has mean and turbulence velocity measurements that appear to be consistent with those measured at the upstream location. The levels and slopes of the data lines at each radius appear connectable between measurement locations. The downstream measurement location is not consistent in the sense that the data lines are not all connectable across the gap between measurement locations. This was not resolved; hence the results from this location downstream should be considered approximate in terms of coordinate reference.

Correlations and spectra for these data sets were computed for reference points nearest the lipline and

at the axial location of maximum difference in turbulence intensities across the shear layer and at the axial location nearest the end of the potential core. For the SP3 jet, these locations are at $x/D = 2.39$ and $x/D = 6.90$ and for the SP7 jet, $x/D = 3.41$ and $x/D = 7.82$. An additional reference point for each jet was at $x/D = 10.0$ in the downstream TR-PIV measurement location. The axial locations for these reference points are marked in Figure 3 for the mean axial velocities near the lipline and in Figure 4 for the axial turbulence intensities.

III. Empirical Mode Decomposition

Empirical mode decomposition (EMD) is an adaptive method to decompose any general non-stationary and nonlinear signal into a set of basis functions known as intrinsic mode functions (IMFs).[4] Flandrin et al.[10] describe the method as one of extracting the local oscillations from the local trend to obtain the IMF. The procedure is defined by an algorithm that is summarized as follows:

1. Identify all maxima and minima of the signal.
2. Interpolate between all maxima and all minima to define an envelope.
3. Compute the average of the envelope at every point in the signal.
4. Subtract the average from the signal to obtain the local oscillations.
5. The local oscillation result is examined to see if it meets the following criteria for an IMF:
   (a) The difference between the number of extrema and the number of zero crossings is at most one.
   (b) The average of the envelope along the signal is zero or near zero according to some convergence criterion.

   If these conditions are not met, the current signal obtained at step 4 is used as the input signal starting at step 1 and the algorithm repeats until the criteria of step 5 are met.

This process extracts one IMF $C_1(t)$ from the signal $u(t)$ leaving a residual $z_1(t)$. The next IMF $C_2(t)$ is then extracted from the residual $z_1(t)$ and so forth until the residual contains one or no extreme value. The complete decomposition of the signal $u(t)$ is achieved with a finite number of IMFs of the order $N \leq \log_2 K$ where K is the number of data points in the signal. The result is written as

$$u(t) = \sum_{n=1}^{N} C_n(t) + z_N(t)\,. \tag{1}$$

An example result of EMD performed on a TR-PIV time history is shown in Figure 5a. The total axial velocity (mean plus fluctuating) is shown as the top signal time history. Prior to performing EMD in this study, the total signal mean value was subtracted from the signal. The first process of removing the local oscillations from the local trend results in the first IMF containing the highest frequency content of the signal. As can be observed, each succeeding IMF contains lower frequency content as the local wavelength between zero crossings in the IMF increases. The residual is near zero since the total signal mean value was removed. Figure 5b shows the IMFs in greater detail over a fraction of the original signal length. The IMFs for a single time history are found to be nearly orthogonal[4] and uncorrelated. Further details and illustrations are given in Appendix A.

The EMD method was developed in general for non-stationary and nonlinear signals and is often applied to signals with significant underlying trends or with short term events. Turbulence measurements such as those presented herein are broadband and approximately stationary in nature though they represent nonlinear behavior in the flow. Flandrin et al.[10] and Wu & Huang[11] discuss the application of EMD to broadband signals. The decomposition of a broadband signal into N IMFs gives a result that represents a signal having been processed by a dyadic filter bank with N filters. A dyadic filter bank is a set of overlapping, band-pass-type filters having a constant band-pass shape with each filter having half or double the frequency range of its neighboring filters. The mean frequencies of the filter bank are given by

$$f_n^c = f_o\, 2^{-n} \tag{2}$$

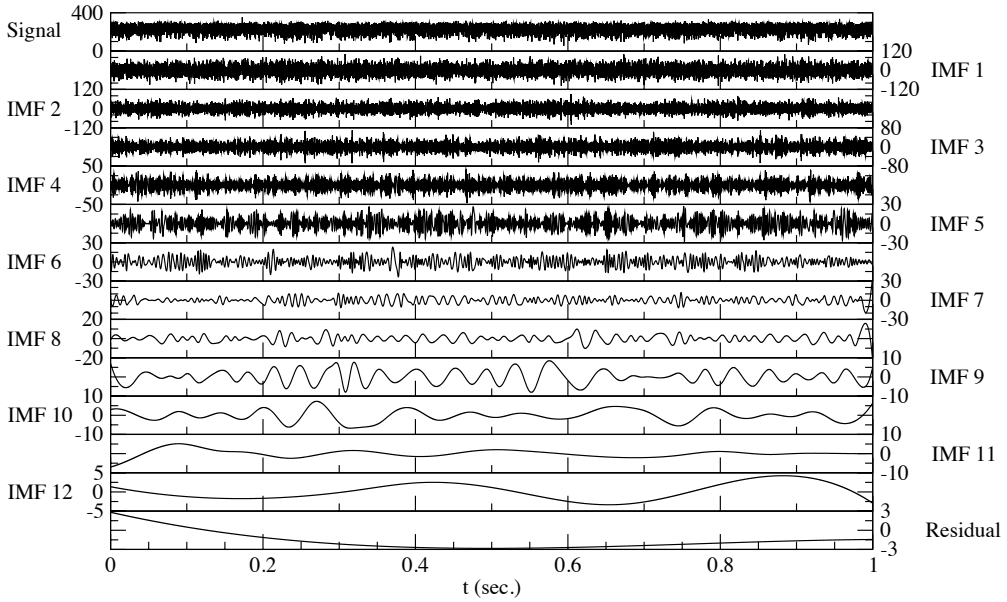

(a) Complete measured time history and IMFs over 1 second.

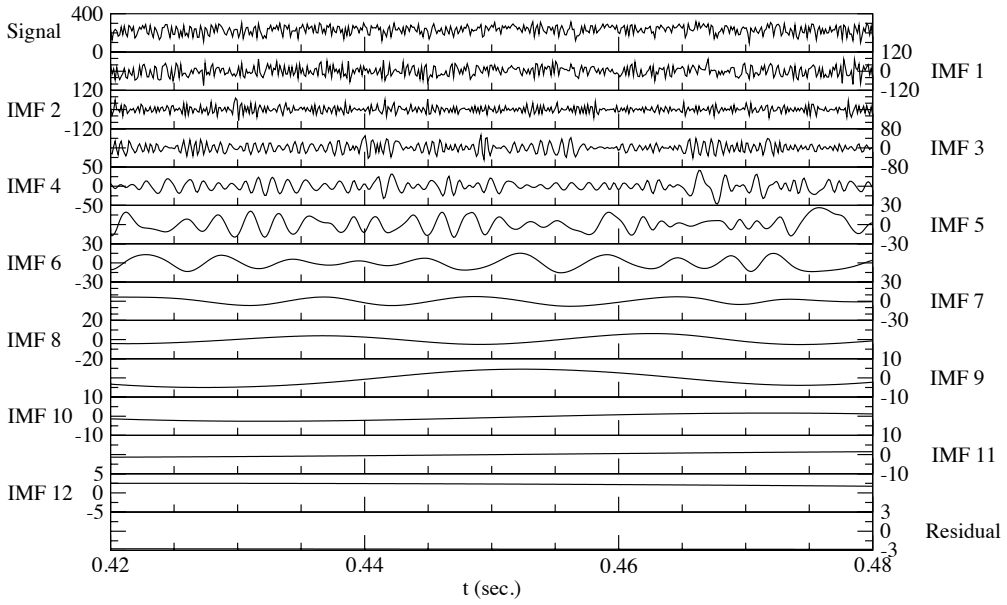

(b) Expanded portion of time history over 0.06 seconds.

Figure 5. Example TR-PIV time history sampled at 25 KHz containing 24993 data points and all the corresponding intrinsic mode functions (IMFs). Data from the shear layer of the SP7 jet with $M_J = 0.98$, $T_t/T_\infty = 1.00$, **at** $x/D = 3.41$ **and** $r/D = -0.49$.

where f_o is a constant and the number 2 is an approximate value. Figure 6a shows the power spectral density computed from the time histories shown in Figure 5 for the total fluctuating signal and each of the first seven IMFs. The spectra for the IMFs show the dyadic filter bank representation for the broadband data processed using EMD. Flandrin et al.[10] noted that there is no predetermination of the bandwidth and location of the filters, but they are automatic and signal dependent. However, for signals that have the same time history length and have similar broadband nature as those obtained from TR-PIV measurements, the filter bank will be similarly located for each signal in terms of the mean frequency and bandwidth of the filters. This is shown in Figures 6b and 6c at locations near the lipline further downstream. The original signal spectrum is recovered when adding the IMFs.[12] This is expected since from equation (1) the IMFs are added in the time domain prior to transforming to the frequency domain. As an illustration, Figure 6

shows the spectra computed after summing IMFs 2 and 3. The spectral level of the total fluctuating velocity is nearly recovered in this region of the spectrum.

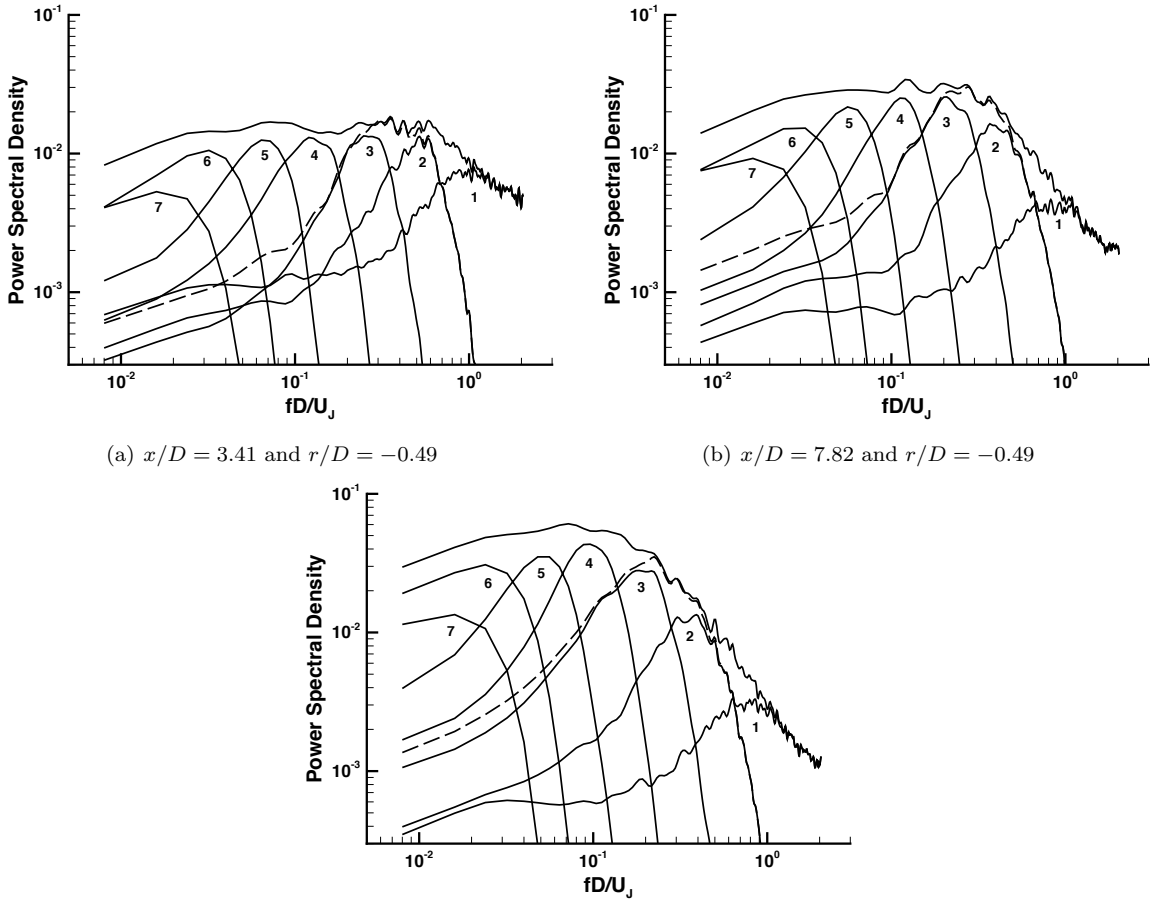

(a) $x/D = 3.41$ and $r/D = -0.49$

(b) $x/D = 7.82$ and $r/D = -0.49$

(c) $x/D = 10.0$ and $r/D = -0.49$

Figure 6. Power spectral densities computed for the axial velocity fluctuations at 3 axial locations near the jet lipline. SP7 jet with $M_J = 0.98$ and $T_t/T_\infty = 1.00$. Highest levels are the total fluctuating velocity spectra. Intrinsic mode function (IMF) spectra are labelled 1 to 7. Dashed lines are spectra for the sum of IMFs 2 and 3.

IV. Correlation Definitions

The data from TR-PIV is arranged as an array of time histories located at discrete points in a plane that cuts across the flow field of the jet. These data may be used to compute both second- and fourth-order, two-point correlations of the velocity fluctuations both for the total fluctuation and for the IMF components. However, the 1 second time histories were too short to obtain sufficient averages for reliable fourth-order correlations. Thus, this paper concentrates on computing second-order correlations. The second-order, two-point correlation is defined over a time length $\mathcal{T}$ by

$$R_{ij}(\boldsymbol{x}, \boldsymbol{\eta}, \tau) = \frac{1}{\mathcal{T}} \int_0^{\mathcal{T}} u_i'(\boldsymbol{x}, t) u_j'(\boldsymbol{x} + \boldsymbol{\eta}, t + \tau)\, \mathrm{d}t \tag{3}$$

where $u_i'(\boldsymbol{x}, t)$ is the total fluctuating velocity (given that the fluctuating velocity is a sum of IMF components) in the i-th direction obtained from the total velocity using $u_i'(\boldsymbol{x}, t) = u_i(\boldsymbol{x}, t) - \overline{u_i(\boldsymbol{x}, t)}$, $\boldsymbol{\eta}$ is the spatial separation, τ is the time delay, and an overbar denotes the time average of the quantity. (From hereon, the term 'total' refers to the total fluctuating velocity.) The normalized two-point correlation or correlation

coefficient is given by

$$r_{ij}(\boldsymbol{x},\boldsymbol{\eta},\tau)=\frac{R_{ij}(\boldsymbol{x},\boldsymbol{\eta},\tau)}{\left[\frac{1}{\mathcal{T}}\int_0^{\mathcal{T}}u_i'(\boldsymbol{x},t)u_i'(\boldsymbol{x},t)\,\mathrm{d}t\,\frac{1}{\mathcal{T}}\int_0^{\mathcal{T}}u_j'(\boldsymbol{x}+\boldsymbol{\eta},t+\tau)u_j'(\boldsymbol{x}+\boldsymbol{\eta},t+\tau)\,\mathrm{d}t\right]^{1/2}} \tag{4}$$

where the denominator integrals are the mean square values of the velocity fluctuations at the two locations in the field.

Generalizing equation (1) for different fluctuating velocity components at each point in space

$$u_i'(\boldsymbol{x},t)=\sum_{n=1}^{N}C_{in}(\boldsymbol{x},t)+z_{iN}(\boldsymbol{x},t)\,, \tag{5}$$

we substitute this into equation (3) and multiply the terms to get the correlation equation that applies after empirical mode decomposition.

$$\begin{aligned}R_{ij}(\boldsymbol{x},\boldsymbol{\eta},\tau)=&\sum_{n=1}^{N}\frac{1}{\mathcal{T}}\int_0^{\mathcal{T}}C_{in}(\boldsymbol{x},t)C_{jn}(\boldsymbol{x}+\boldsymbol{\eta},t+\tau)\,\mathrm{d}t+\sum_{n=1}^{N}\frac{1}{\mathcal{T}}\int_0^{\mathcal{T}}C_{in}(\boldsymbol{x},t)\sum_{k\neq n}^{N}C_{jk}(\boldsymbol{x}+\boldsymbol{\eta},t+\tau)\,\mathrm{d}t\\&+\sum_{n=1}^{N}\frac{1}{\mathcal{T}}\int_0^{\mathcal{T}}z_{iN}(\boldsymbol{x},t)C_{jn}(\boldsymbol{x}+\boldsymbol{\eta},t+\tau)\,\mathrm{d}t+\sum_{n=1}^{N}\frac{1}{\mathcal{T}}\int_0^{\mathcal{T}}C_{in}(\boldsymbol{x},t)z_{jN}(\boldsymbol{x}+\boldsymbol{\eta},t+\tau)\,\mathrm{d}t\\&+\frac{1}{\mathcal{T}}\int_0^{\mathcal{T}}z_{iN}(\boldsymbol{x},t)z_{jN}(\boldsymbol{x}+\boldsymbol{\eta},t+\tau)\,\mathrm{d}t\end{aligned} \tag{6}$$

This equation is also normalized as in equation (4), thus all the normalized correlations involving the IMFs are relative to the root mean square values of the total fluctuating velocities at the two locations.

To compute the length and time scales from the normalized, two-point correlation, we follow the approach of Kerhervé et al.[13] The integral length scale is computed from

$$\Lambda_{ij}^{k}(\boldsymbol{x})=\int_0^{+\infty}r_{ij}(\boldsymbol{x},\eta_k,\tau=0)\,\mathrm{d}\eta_k \tag{7}$$

and the integral time scale by

$$\tau_{ij}^{k}(\boldsymbol{x})=\int_0^{+\infty}r_{ij}(\boldsymbol{x},\eta_k=U_{ck}\tau,\tau)\,\mathrm{d}\tau \tag{8}$$

where U_{ck} is the phase speed in the η_k direction. These scales are determined for signals that either contained all the frequency content of the total fluctuating velocity or the band-pass frequency content of the individual IMFs. To determine the frequency dependence of these scales, Kerhervé et al.[13] used the complex coherence function. This function is computed using the Fourier transform with respect to the time delay of equation (3), the cross-power spectral density function, and the Fourier transforms of the velocity correlations at the two points in the field. See Kerhervé et al.[13] for the details. The final results for the frequency dependent length scale and the frequency dependent time scale are

$$\Lambda_{ij}^{k}(\boldsymbol{x},\omega)=\int_0^{+\infty}\Re\left\{\gamma_{ij}(\boldsymbol{x},\eta_k,\omega)\right\}\,\mathrm{d}\eta_k \tag{9}$$

and

$$\tau_{ij}^{k}(\boldsymbol{x},\omega)=\frac{1}{u_{ck}(\omega)}\int_0^{+\infty}\left|\gamma_{ij}(\boldsymbol{x},\eta_k,\omega)\right|\,\mathrm{d}\eta_k \tag{10}$$

where, following Morris & Zaman,[14]

$$u_{ck}(\omega)=\omega/|\partial\phi(\eta_k,\omega)/\partial\eta_k|, \tag{11}$$

γ_{ij} is the complex coherence function, $\Re$ denotes the real part, and $\phi(\eta_k,\omega)$ is the phase of the complex coherence function.

The approximately 1 second of data obtained from the TR-PIV measurements provided time histories containing 24993 samples. The calculation of the correlations and spectra were performed following procedures given in Bendat & Piersol.[15] The time histories were divided into equal length segments. Each segment was windowed using a Kaiser-Bessel window (parameter $\alpha = 3.0$), zero padded, and then processed by the fast Fourier transform. The segment transforms were summed and averaged to obtain auto- and cross-spectra. These were then inverse Fourier transformed to obtain the auto- and cross-correlations. With a fixed time history length, a trade-off has to be made between good frequency resolution and low variance.[16] For this study, the time histories were divided into 194 segments with 256 points each with 50% overlap. This resulted in a frequency resolution of 48.8 Hz for spectrum estimates with a standard deviation of 8%.

V. Results

The velocity time histories at each point in the frame of TR-PIV data are decomposed into IMFs that are used to compute the second-order, two-point correlation of equation (6) normalized as in equation (4). The last three terms in equation (6) are correlations involving the residual of the decomposition. Figure 5 shows the residual to be relatively small and nearly constant compared to most IMFs. Consequently, the integral involving residuals is small and the integrals involving residuals and IMFs are nearly zero. The latter follows from removing the nearly constant residual from the integral resulting in a computation of the average intrinsic mode value which is zero. Of the remaining two integrals, we will concentrate in this paper on computing the first integral; the second-order, two-point correlation of IMFs of the same mode number.

Contour plots of $r_{11}(\boldsymbol{x}, \eta_1, \tau)$, the correlation between fluctuating axial velocity components, are shown in Figures 7 to 12 for the total fluctuating axial velocity and the first 5 IMFs from the two jets listed in Table 1 at the three reference points. The correlations are shown as a function of the normalized axial separation η_1/D and the normalized delay time $\tau U_J/D$. All the correlation plots are on the same contour scale from -0.1 to 1.0, thus the IMF correlation levels are relative to the total fluctuating velocity correlation level. A computed elliptic contour is included in the figures. These will be defined in the next paragraph. The IMF correlations all follow the same pattern. The highest frequency intrinsic mode IMF 1 is confined to a small region of space and time. As the frequency decreases with increasing IMF mode number, the correlation broadens in both space and time. There is also a noticeable change in the slope of the contours with IMF indicating a change in phase velocity with frequency. Two issues affect the results obtained from these correlations. The first is a lack of spatial grid points to properly resolve the rapid changes in the correlations in the high frequency IMF 1, especially in the lower velocity SP3 jet. The second is manifest as an anomaly visible in the contour plots at $\eta_1/D = 0$ and centered on $\tau U_J/D = 0$. It is especially visible in the generally lower contour levels in the higher number IMFs. It occurs within plus or minus one spatial grid point of $\eta_1/D = 0$. Some results were affected by this as discussed below.

To extract phase velocity and scale values from the correlation results, we fit an ellipse to a contour of the data,[3] shown as the black line shape in Figures 7 to 12. The contour chosen was 1/e times the correlation peak $r_{11}(\boldsymbol{x}, 0, 0)$ for the total fluctuating axial velocity or the individual IMFs. Assuming the correlation is monotonically decreasing, such as an exponential or Gaussian shaped function, an estimate for the integral length scale, $L_\eta = \Lambda^1_{11}$, following equation (7), was found. The distance is from the reference point, the origin in the $(\eta_1/D, \tau U_J/D)$ plane, to the ellipse along η_1/D at $\tau U_J/D = 0$. Similarly, the integral time scale, $\tau_\eta = \tau^1_{11}$, equation (8), was estimated using the distance from the reference point to the ellipse along the line $\eta_1/D = (U_c/U_J)(\tau U_J/D)$. The phase velocity U_c/U_J was also determined from the ellipse equation. The details of this ellipse method are given in Appendix B. An advantage of this method is that it allows scale estimates to be made where measured data is lacking. For example, Figure 11a shows that the reference point is too close to the downstream edge of the measurement frame to allow the correlation to decay sufficiently along the constant phase velocity line to obtain an estimate for the integral time scale. However, with the ellipse equation determined from fitting the available data, an estimate for the time scale can be computed. The results using this method to estimate the phase velocities and the integral length and time scales are shown in Table 2 for the SP3 jet and in Table 3 for the SP7 jet. For reference, the mean axial velocities at the reference points are included in the tables. The values missing in the tables are due to the ellipse method giving unreliable results. Especially at the shear layer reference point and for higher number IMFs, the presence of the anomaly affects the location of the ellipse fitting points, skewing the tilt of the ellipse and affecting the length of the ellipse axes. Thus, the extracted values based on the ellipse method were inaccurate. As a check of the method in general, we compare the total fluctuating

x/D		Total	IMF 1	IMF 2	IMF 3	IMF 4	$\overline{u}/U_J$
2.39	U_c/U_J	0.705	–	–	–	–	0.756
	L_η/D	0.108	–	–	–	–	
	$\tau_\eta U_J/D$	0.408	–	–	–	–	
6.90	U_c/U_J	0.564	0.709	0.580	0.550	0.478	0.594
	L_η/D	0.388	0.061	0.137	0.287	0.509	
	$\tau_\eta U_J/D$	3.148	0.135	0.567	1.686	2.633	
10.0	U_c/U_J	0.529	0.623	0.541	0.498	0.480	0.548
	L_η/D	0.459	0.064	0.144	0.299	0.529	
	$\tau_\eta U_J/D$	3.638	0.142	0.655	1.480	3.089	

Table 2. Integral properties from correlations for the total fluctuating velocity and IMF components at three axial locations near the lipline $r/D = -0.49$ using the ellipse method. SP3 jet. Phase velocity, U_c. Integral length scale, L_η. Integral time scale, τ_η. Mean axial velocity, $\overline{u}$.

velocity results in Table 3 for the SP7, cold, $M_J = 0.9$ jet to those values found by Kerhervé et al.[13] for an isothermal, $M_J = 0.9$ jet on the lipline near the end of the potential core. Using Table 3 at $x/D = 7.82$, we get $U_c = 185\,\text{m/s}$, $L_\eta = 18.6\,\text{mm}$, and $\tau_\eta = 0.50\,\text{ms}$. The Kerhervé et al.[13] values are $U_c = 137\,\text{m/s}$, $L_\eta = 19\,\text{mm}$, and $\tau_\eta = 0.62\,\text{ms}$. These results show that the ellipse method can produce correlation-based phase velocity and scale values comparable with other methods. The assumption here is that the correlation in this part of the flow follows an exponential or Gaussian shape implying little or no significant oscillations in the tail of the correlation.

Within the limitations of the frequency range of the measurements and the nature of empirical mode decomposition, the IMF 1 values in Tables 2 and 3 represent the measured small-scale turbulent phase velocity and integral scales. Though the comparison is qualitative, since the measurements here are near the lipline of an axisymmetric jet, a couple of trends are similar to those found by Bodony & Lele[3] from the computed results for a two-dimensional shear layer. One is that the total turbulence phase velocities are less than the mean velocities on the higher-speed side of the shear layer and that the small-scale phase velocities may be higher (and in this case are higher) than the total phase velocities. The other is that the small-scale integral scales are much smaller than the total fluctuating velocity integral scales. The computed shear layer small-scale integral scales are 60 to 80% smaller in the downstream portion of the shear layer. For the two jet cases here, the small-scale integral scales are 80 to 95% smaller.

Given that the intrinsic mode functions isolate a range of frequencies that decrease in frequency as the IMF mode number increases, the turbulent phase velocity and scale values listed in Tables 2 and 3 show the gross changes in these values with frequency. The phase velocity decreases with decreasing frequency and

x/D		Total	IMF 1	IMF 2	IMF 3	IMF 4	$\overline{u}/U_J$
3.41	U_c/U_J	0.687	0.769	0.540	0.396	–	0.747
	L_η/D	0.162	0.090	0.172	0.252	–	
	$\tau_\eta U_J/D$	0.984	0.245	0.529	0.807	–	
7.82	U_c/U_J	0.596	0.670	0.586	0.540	0.384	0.626
	L_η/D	0.366	0.076	0.206	0.375	0.545	
	$\tau_\eta U_J/D$	3.057	0.403	1.036	2.246	2.266	
10.0	U_c/U_J	0.568	0.644	0.562	0.535	0.460	0.592
	L_η/D	0.433	0.090	0.215	0.401	0.684	
	$\tau_\eta U_J/D$	3.606	0.280	1.089	2.314	3.476	

Table 3. Integral properties from correlations for the total fluctuating velocity and IMF components at three axial locations near the lipline $r/D = -0.49$ using the ellipse method. SP7 jet. Phase velocity, U_c. Integral length scale, L_η. Integral time scale, τ_η. Mean axial velocity, $\overline{u}$.

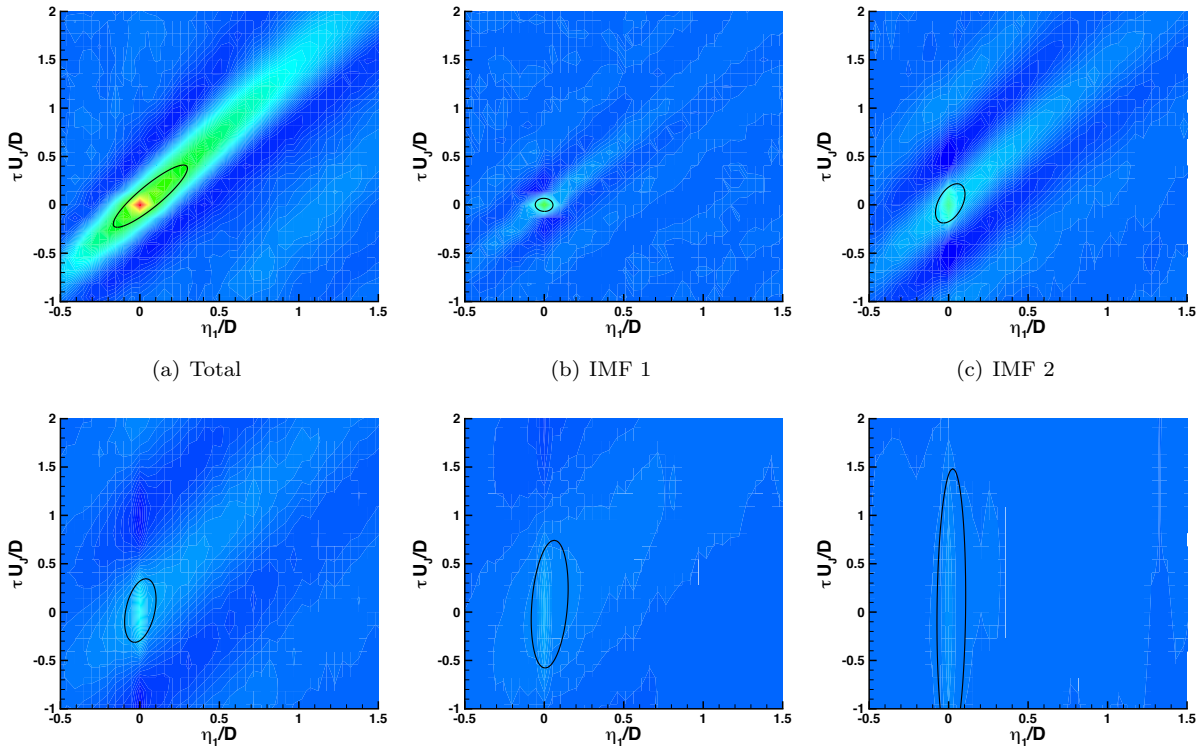

(a) Total (b) IMF 1 (c) IMF 2

(d) IMF 3 (e) IMF 4 (f) IMF 5

Figure 7. Contours of r_{11} in the SP3 jet for the total fluctuating velocity and intrinsic mode functions (IMF) 1 to 5. Reference point $x/D = 2.39$ and $r/D = -0.49$. Black line is the computed ellipse.

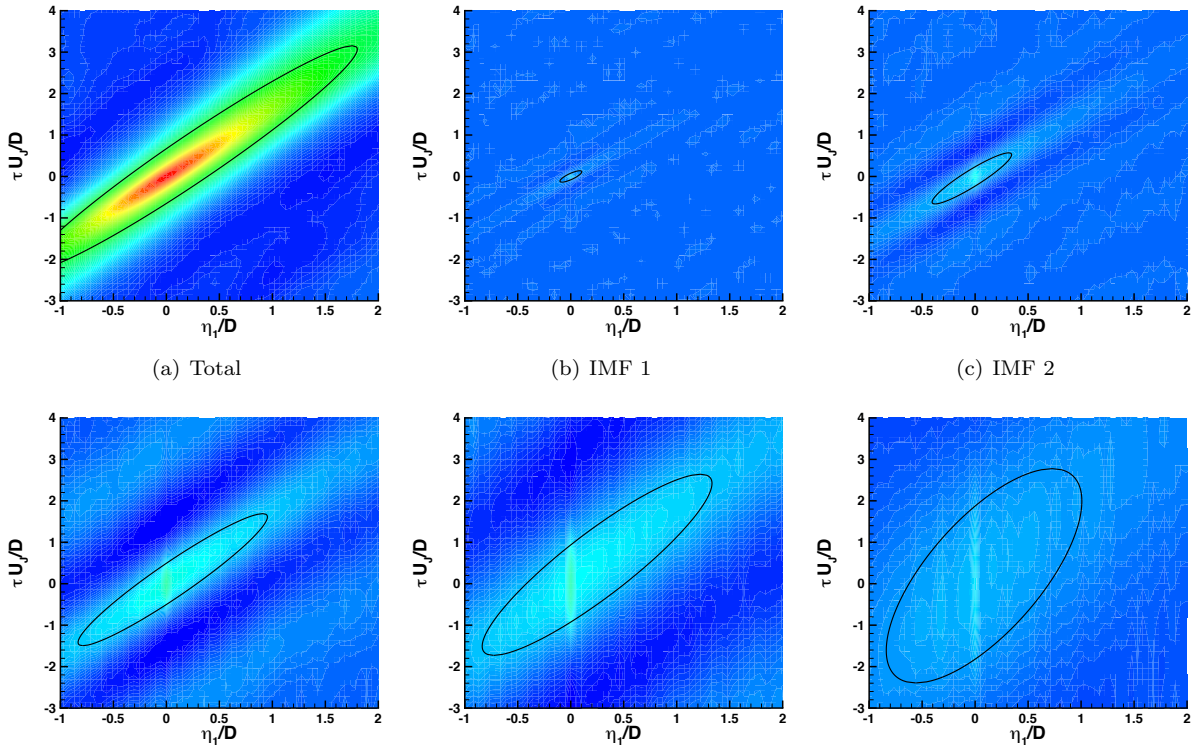

(a) Total (b) IMF 1 (c) IMF 2

(d) IMF 3 (e) IMF 4 (f) IMF 5

Figure 8. Same caption as Figure 7 with $x/D = 6.90$.

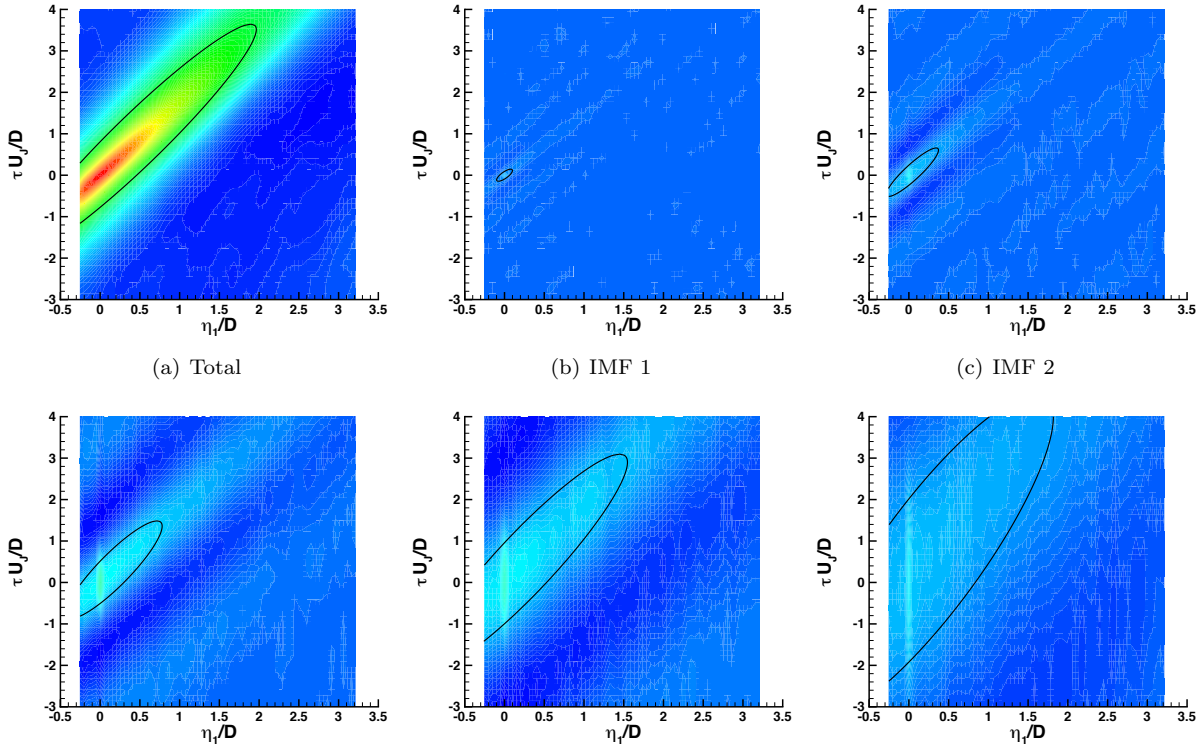

(a) Total (b) IMF 1 (c) IMF 2

(d) IMF 3 (e) IMF 4 (f) IMF 5

Figure 9. Same caption as Figure 7 with $x/D = 10.0$.

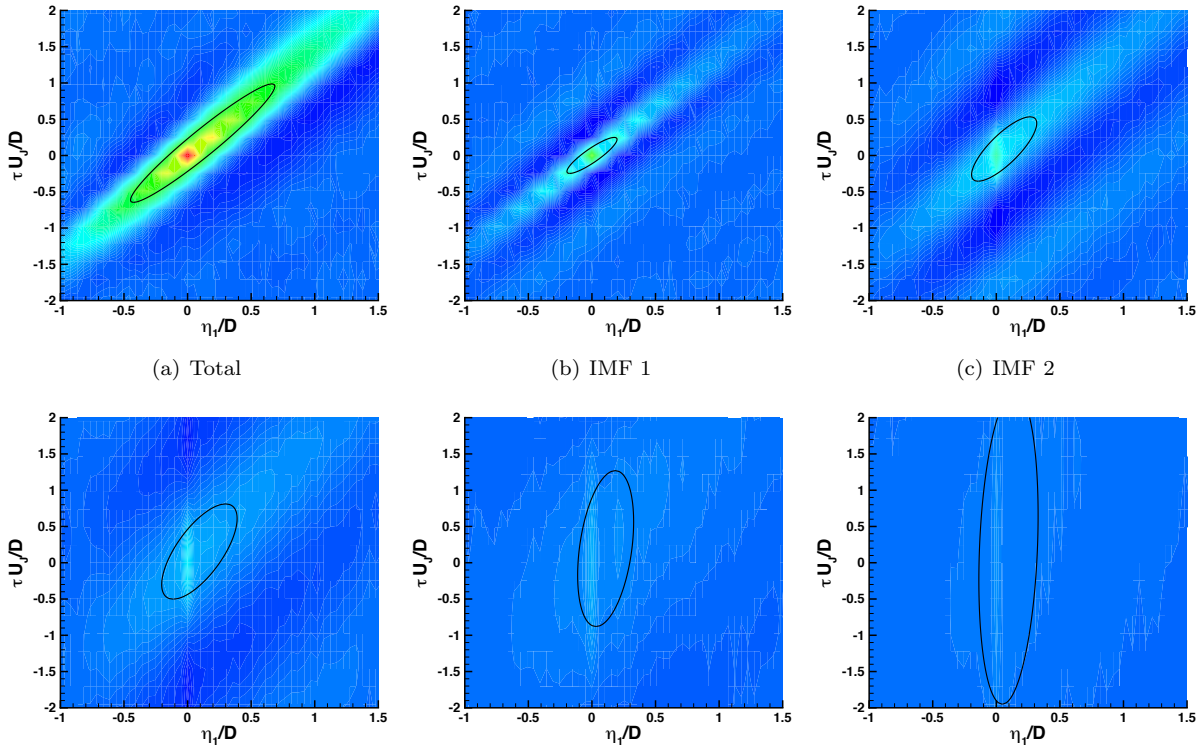

(a) Total (b) IMF 1 (c) IMF 2

(d) IMF 3 (e) IMF 4 (f) IMF 5

Figure 10. Contours of r_{11} in the SP7 jet for the total fluctuating velocity and intrinsic mode functions (IMF) 1 to 5. Reference point $x/D = 3.41$ and $r/D = -0.49$. Black line is the computed ellipse.

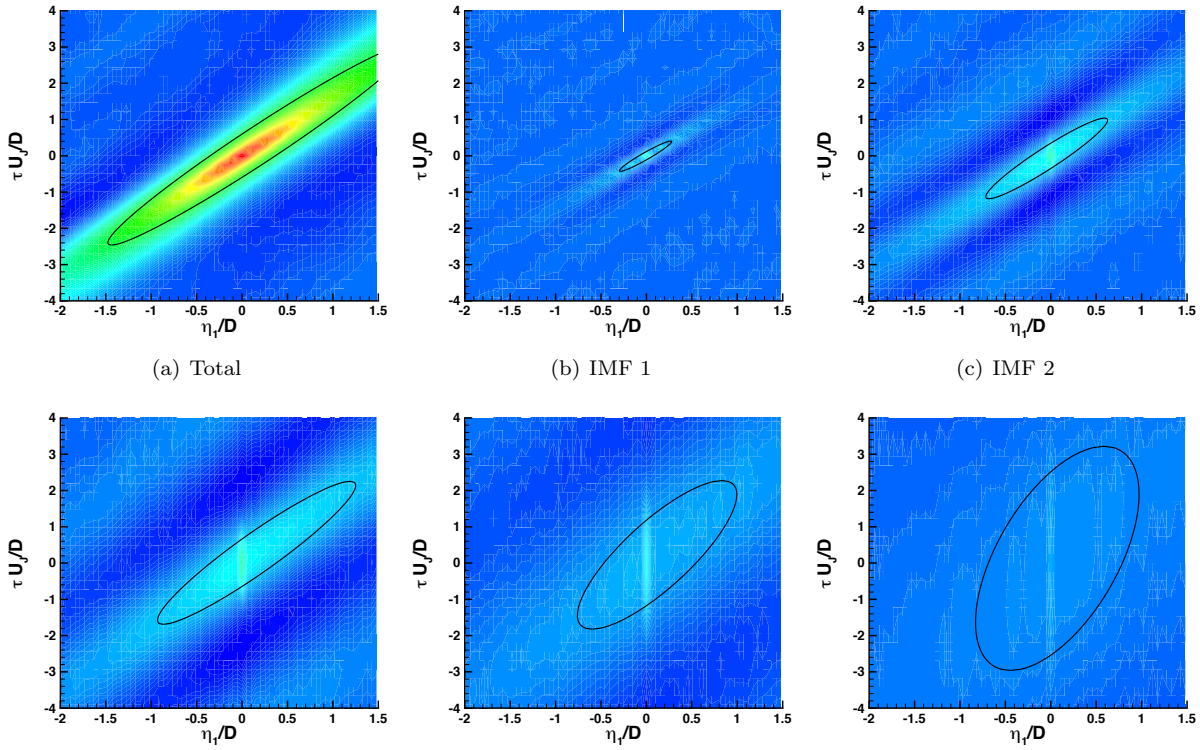

(a) Total (b) IMF 1 (c) IMF 2

(d) IMF 3 (e) IMF 4 (f) IMF 5

Figure 11. Same caption as Figure 10 with $x/D = 7.82$.

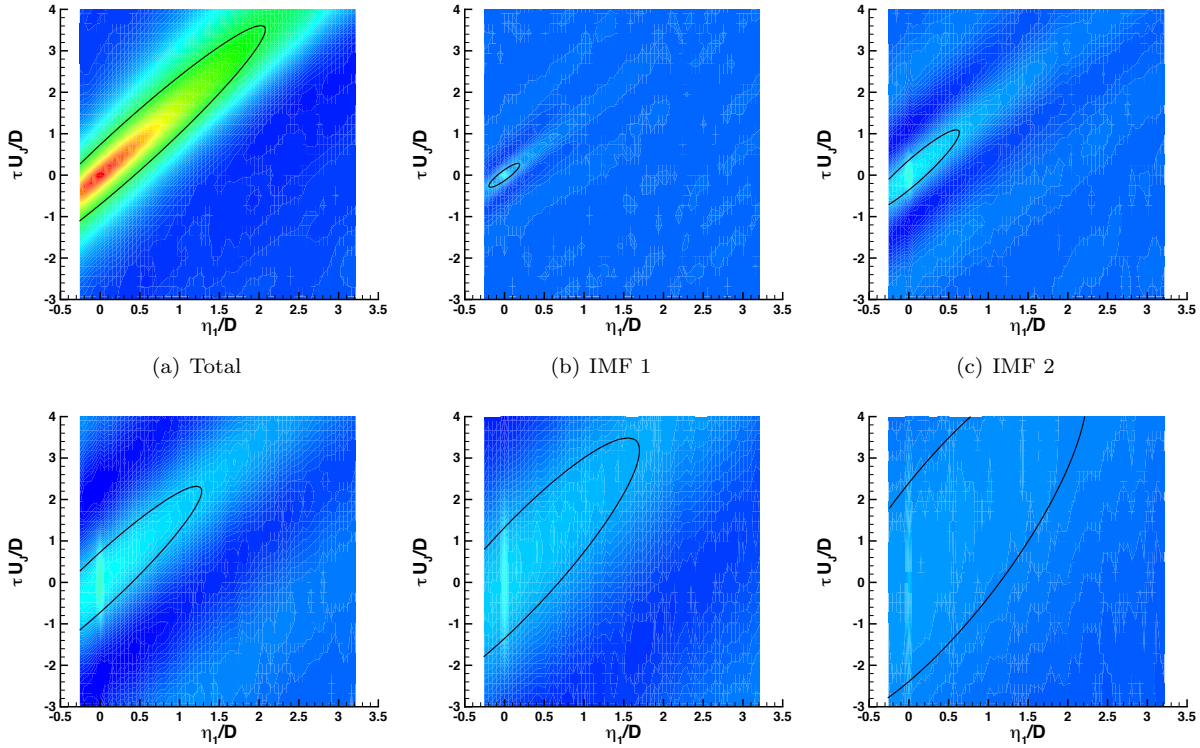

(a) Total (b) IMF 1 (c) IMF 2

(d) IMF 3 (e) IMF 4 (f) IMF 5

Figure 12. Same caption as Figure 10 with $x/D = 10.0$.

the integral length and time scales have smaller values at the high frequency (IMF 1) and increase in scale at progressively lower frequencies (higher IMF mode number). We next compare these results to those obtained for the frequency dependent length scale and the frequency dependent time scale following equations (9) and (10), respectively.

The ability to compute the integrals in equations (9) and (10) without modeling the measured data is very difficult as noted by Kerhervé et al.[13] In equation (9), the real part of the complex coherence decays slowly at low frequency with separation distance from the reference point and then begins to oscillate at large distances. As the frequency increases, the oscillations move closer to the reference point and may increase in intensity. Hence, within the limited spatial measurement frame, the spatial integration does not converge using only the measured data. Equation (10) uses the magnitude of the complex coherence which tends to only decay away from the reference point. Thus, above some frequency, the measurement space is large enough so that the integral should converge. Since the use of equation (9) with measured data is not possible, we use the decay of the complex coherence magnitude to estimate the frequency dependent length and time scales. Following Harper-Bourne[17] and Morris & Zaman,[14] the length scale is given by the distance at which the complex coherence magnitude $|\gamma_{ij}(\boldsymbol{x}, \eta_1, \omega)|$ decays by 1/e. (We acknowledge that Kerhervé et al.[13] consider this to be a poor estimate.) For the time scale, we use the point at which the value $|\gamma_{ij}(\boldsymbol{x}, \eta_1, \omega)|/u_c(\omega)$ decays by 1/e. The frequency dependent phase velocity is computed directly from the phase of the complex coherence using equation (11). The results are shown in Figures 13 to 15 for the SP7 jet at the three axial locations near the jet lipline.

Figure 13 shows the frequency dependent phase velocities. The results computed for the IMFs are shown in the peak region of the band-pass filter given approximately by the frequency range from $f_n^c\, 2^{-1/2}$ to $f_n^c\, 2^{1/2}$, where f_n^c is given by equation (2), except for IMF 1 which has the same upper frequency limit as the total fluctuating velocity. The phase velocities for IMF 1 and IMF 2 follow closely the phase velocity for the total fluctuating velocity except at the edges of the filter range. More scatter is found in the results for lower frequency IMFs 3 and 4 due in part to both insufficient frequency resolution and averaging. The color horizontal lines are the phase velocity values from Table 3 that were derived from the correlation results. The correlation derived phase velocities more accurately coincide with the frequency dependent results at the higher frequencies and at the downstream locations. The final comparison shows that the data follows the curve fit equation from Morris & Zaman[14]

$$\frac{U_c}{U_J} = 0.062 \ln\left(\frac{fD}{U_J}\right) + 0.701 \tag{12}$$

that has slightly different coefficients compared to the Harper-Bourne[17] version of this equation. The data from each of these locations in the SP7 jet would give slightly different fit slopes and offset values, but the basic form of the equation would be the same.

The estimated frequency dependent length scales are shown in Figure 14. The basic trend is for the length scale to be somewhat constant at the low frequency followed by a decrease in length scale as frequency increases. These results follow those of Morris & Zaman[14] in that the Strouhal number where the length scale

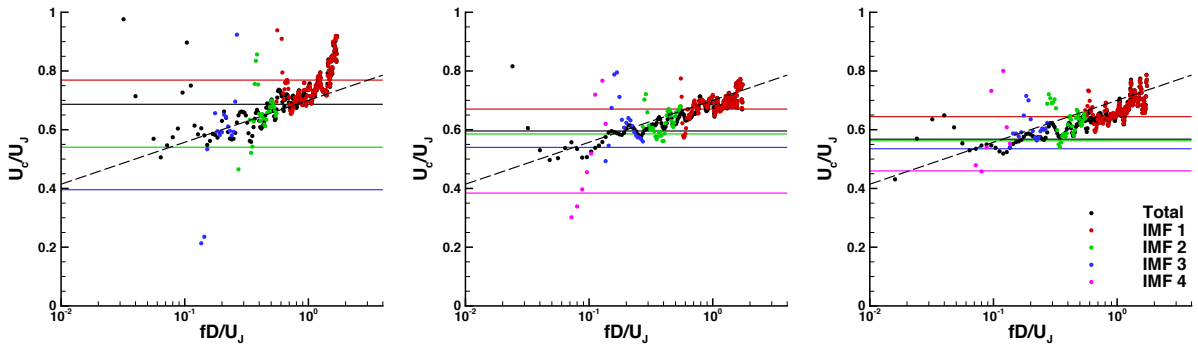

(a) $x/D = 3.41$ (b) $x/D = 7.82$ (c) $x/D = 10.0$

Figure 13. Phase velocity SP7 jet with $M_J = 0.98$ and $T_t/T_\infty = 1.00$ at 3 axial locations near the lipline $r/D = -0.49$. Symbols are frequency dependent phase velocities. Horizontal lines are correlation based phase velocities, eq. (16). Dashed line is eq. (12).

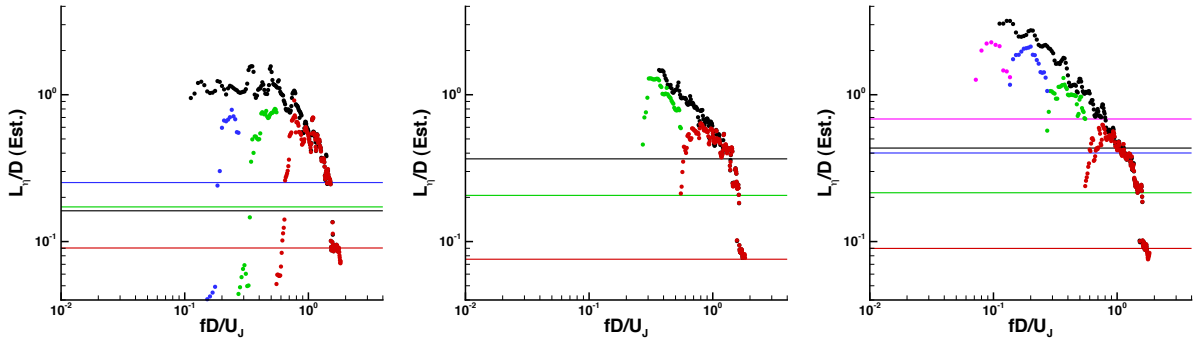

(a) $x/D = 3.41$ (b) $x/D = 7.82$ (c) $x/D = 10.0$

Figure 14. Length scale SP7 jet with $M_J = 0.98$ and $T_t/T_\infty = 1.00$ at 3 axial locations near the lipline $r/D = -0.49$. Symbols are frequency dependent length scales. Horizontal lines are correlation based integral length scales, eq. (14). See Fig. 13c for legend.

changes from constant to a decreasing value moves to a lower value as the reference point moves downstream. At the end of the potential core location shown in Figure 14b, there is insufficient axial extent to enable the computation of the lower Strouhal number length scales. The IMF results follow those for the total fluctuating velocity, though the estimates for the length scale are lower for IMFs 2 to 4. A possible reason for this will be discussed in the next section. A comparison of these results with the correlation integral length scale (horizontal lines for the values from Table 3) may indicate that the estimates for the frequency dependent length scale are too high. The oscillations inherent in the real part of the complex coherence would provide cancellations in the calculation of equation (9) resulting in smaller length scales that would coincide more closely with the integral length scales.

Figure 15 shows the frequency dependent time scale for the total fluctuating velocity and the IMFs where there is sufficient data in the axial direction to make the calculation. The comparisons with the integral time scales are closer in value than found for the length scale comparison in Figure 14. Again, the IMF results follow the total fluctuating velocity results with more scatter in IMFs 2 to 4 especially in the shear layer. The accuracy of computing the integral time scale using the ellipse method was estimated for the IMF 1 and IMF 2 results shown in Figure 15c. The 1/e point was found by interpolation along the constant phase velocity line of r_{11}. The results are given by the dashed lines in the figure. For IMF 1, the directly computed integral time scale is 33% higher than the ellipse method time scale. With better resolution at IMF 2, the difference decreases to 11%.

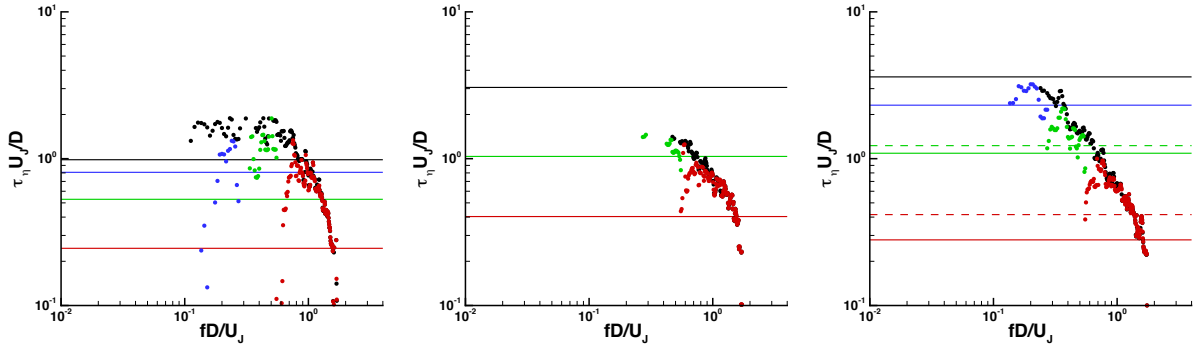

(a) $x/D = 3.41$ (b) $x/D = 7.82$ (c) $x/D = 10.0$

Figure 15. Time scale SP7 jet with $M_J = 0.98$ and $T_t/T_\infty = 1.00$ at 3 axial locations near the lipline $r/D = -0.49$. Symbols are frequency dependent time scales. Horizontal lines are correlation based integral time scales, eq. (15). See Fig. 13c for legend.

VI. Discussion

The results shown in the previous section are based on accepting that the IMFs of different mode numbers are nearly uncorrelated at a point and assuming that the neighboring point IMFs of different mode numbers are also uncorrelated. In this section, we will infer that the latter assumption is generally incorrect and that the second term on the right side of equation (6) cannot be ignored. This term represents all the two-point, cross-correlations in space and time between IMFs having different mode numbers. Figure 16a shows the individual two-point correlation as a function of the time delay at zero spatial separation for each IMF up to IMF 8 and the corresponding correlation for the total fluctuating velocity. The correlations are all normalized the same, as given in equation (4), to show the level of correlation among each individual IMF relative to the total fluctuating velocity correlation. Figure 16b shows incremental results from summing the correlations shown in Figure 16a. The IMF correlations sum to recover the total fluctuating velocity correlation at zero time delay which follows from the IMFs being orthogonal. However, when temporal delay occurs the individual IMF correlations no longer add to completely obtain the total fluctuating velocity correlation. The small difference between the total and the summed correlations indicates the the IMFs in this case are nearly uncorrelated at a point in space but not completely uncorrelated. Figure 17 shows that a small spatial separation between the two measurement points results in a much larger difference between the summed individual IMF correlations and the total fluctuating velocity correlation. The summed correlation reaches a peak that is 60% of the total correlation peak. Clearly, cross-correlations of IMFs with different

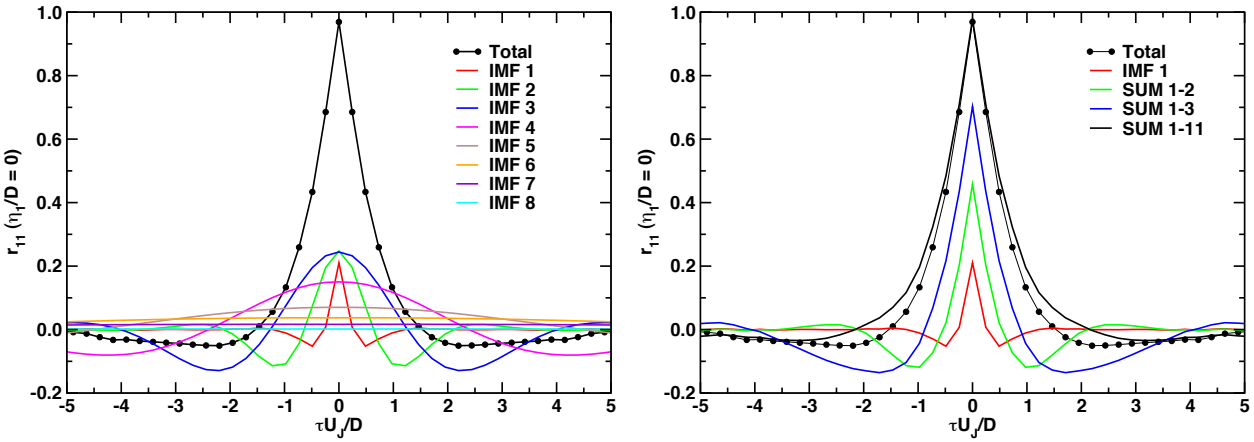

(a) Total and individual IMF

(b) Summation of IMF correlations

Figure 16. Example r_{11} correlations as a function of the temporal separation with both measurement locations at the reference point. SP7 jet. Reference point $x/D = 7.82$ and $r/D = -0.49$.

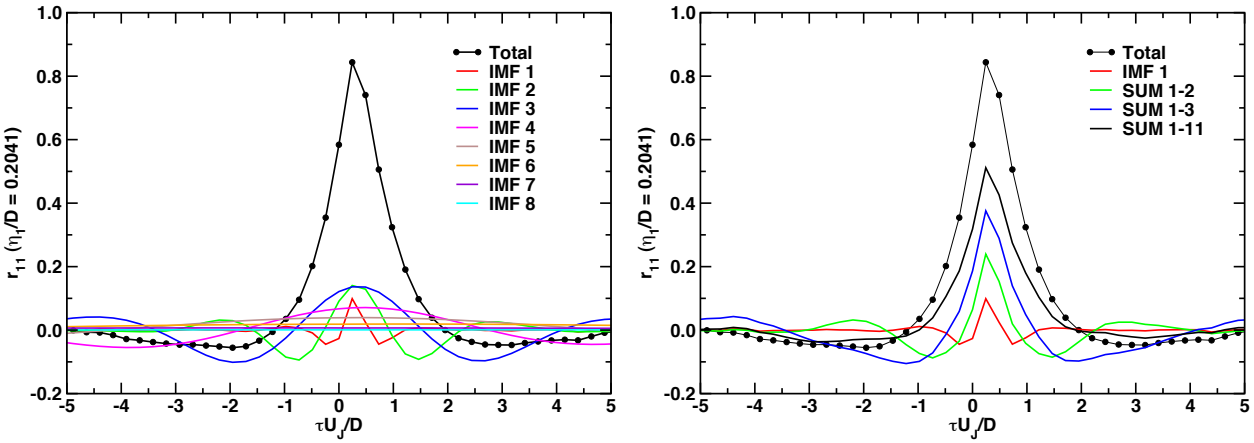

(a) Total and individual IMF

(b) Summation of IMF correlations

Figure 17. Example r_{11} correlations as a function of the temporal separation with the measurement locations separated by $\eta_1/D = 0.2041$. SP7 jet. Reference point $x/D = 7.82$ and $r/D = -0.49$.

mode numbers are required to make up the difference. Further examples of correlations as a function of the axial spatial separation are shown in Figure 18 for zero time delay and in Figure 19 for a small time delay between measurement points. The requirement for including IMF cross-correlation terms is clearly evident as the sum of the individual IMF correlations falls short of the total fluctuating velocity correlation.

The consequence of neglecting the cross-correlations between IMFs of different mode numbers can also be found in the phase velocity and scale results in Figures 13 to 15. For IMF 1, the effects appear to be small in the range of Strouhal number 1 to 2, the upper half of the measured frequency range. The total fluctuating velocity and IMF 1 results are in basic agreement. The IMF cross-correlation terms are not as important for the IMF 1 results except near the lower end of the frequency range. The IMF 2 to 4 results occur in increasingly narrower frequency bands resulting in deviations in the phase velocities and decreases in the length and time scales compared to the total fluctuating velocity results. In Figure 14, the frequency dependent length scales of IMFs 2 to 4 are smaller than the corresponding length scales for the total fluctuating velocity. The difference comes from the neglected cross-correlation terms that pass through the linear process of Fourier transforming equation (6) and taking the real part in equation (9). The differences in the frequency dependent time scales are more difficult to discern since taking the magnitude of the complex coherence function, equation (10), is not a linear process.

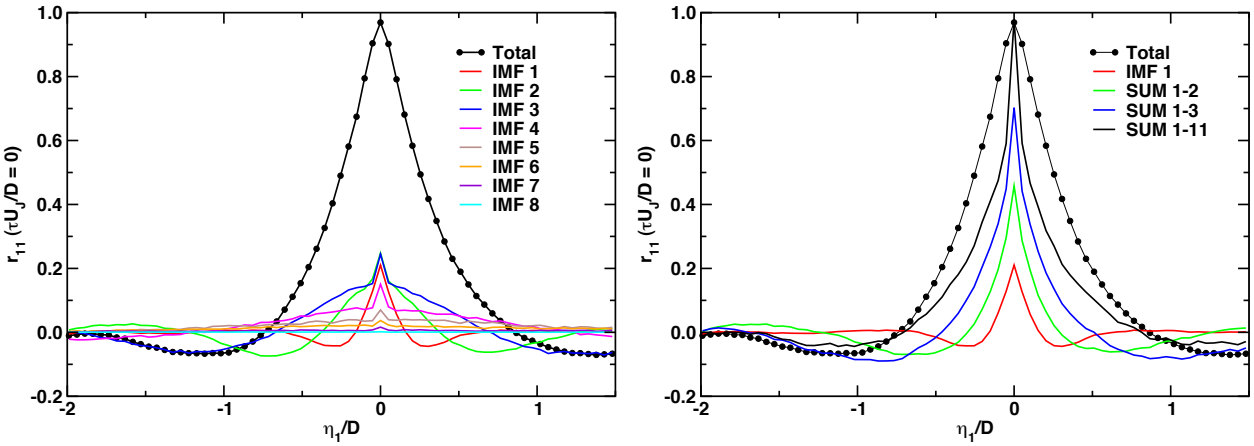

(a) Total and individual IMF

(b) Summation of IMF correlations

Figure 18. Example r_{11} correlations as a function of the axial spatial separation with no time delay between measurement locations. SP7 jet. Reference point $x/D = 7.82$ and $r/D = -0.49$.

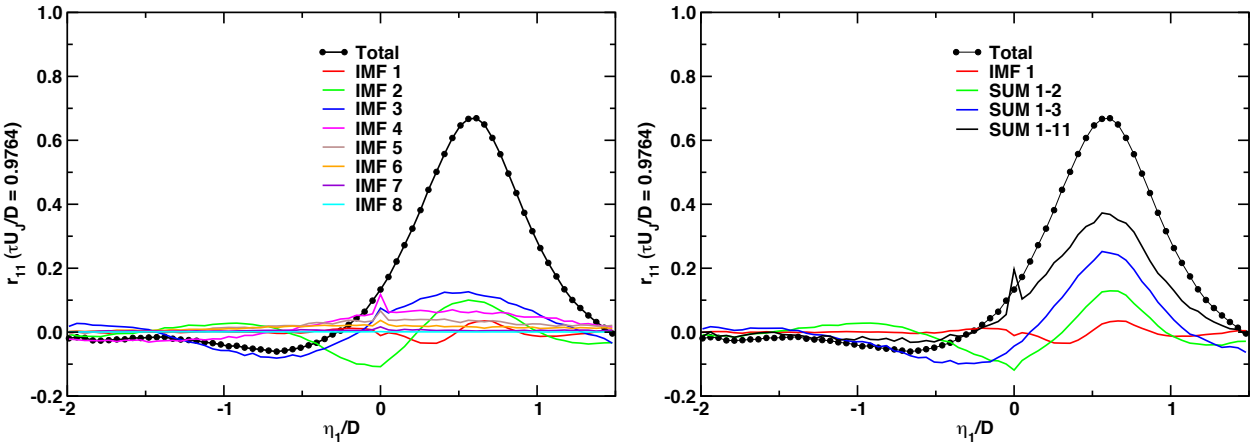

(a) Total and individual IMF

(b) Summation of IMF correlations

Figure 19. Example r_{11} correlations as a function of the axial spatial separation with a time delay of $\tau U_J/D = 0.9764$ between measurement locations. SP7 jet. Reference point $x/D = 7.82$ and $r/D = -0.49$.

VII. Concluding Remarks

A new application of the empirical mode decomposition (EMD) method has been shown in this paper. Instead of analyzing a single time history signal or a small set of time histories, a large array of closely spaced time histories derived from TR-PIV measurements have been analyzed. The results from EMD were equivalent to passing the time histories through a bank of band-pass filters. This data was then used in two-point correlation calculations resulting in the determination of turbulence phase velocities and length and time scales that only apply to a particular band-pass range. The highest frequency-range results may be applicable to subgrid scale noise source modeling.

Some issues were identified that would need to be resolved to better use the method.

- A higher sampling rate would increase the Strouhal number range that can be analyzed and/or allow higher speed jets to be studied.
- The length of the time histories needs to be increased. This would allow for greater frequency resolution and/or allow a larger number of averages to be performed to reduce spectral variance and allow better results for fourth-order correlation calculations.
- There needs to be finer spatial resolution in the TR-PIV measurements. The higher frequency correlations can change rapidly in a short distance.

Unfortunately, hardware limitations may inhibit significant improvements in any of these issues.

Finally, there is the issue of the importance of the cross-correlation of IMFs of different mode numbers. Since the IMFs represent data in overlapping frequency bands, it is not yet known if these space-time cross-correlations are between different frequency data or between the same frequencies in the overlapping regions. The fact that the highest frequency IMF 1 results appeared not to deviate much from the total results except at the low end of the frequency range suggests the latter explanation for the results. The lower frequency IMFs have overlap on both ends of the band-pass filter with results showing that the cross-correlation information is missing. Resolving these matters is part of future work.

Appendix A – Some Details of Empirical Mode Decomposition

Further details about the empirical mode decomposition (EMD) method as applied in this study are given in this appendix. Specifically, information is given about interpolation and sifting, stopping criteria, and boundary conditions that were used in the current work. Any issues related to these are discussed in the references cited below

Empirical Mode Decomposition

The EMD method may be applied to any general, non-stationary, and nonlinear signal.[4] The signal $u(t)$ is sampled to create a set $u(i)$ where $i = 1, 2, \ldots, K$. We start by identifying the extrema of $u(i)$, the positive peaks and the negative peaks in our case since the mean value of the signal is removed from the signal prior to decomposition. The positive peaks are used to construct an interpolating function $e_{max}(i)$ using a cubic spline. Similarly, the negative peaks are used to construct the interpolating function $e_{min}(i)$. The original signal $u(i)$ and $e_{max}(i)$ and $e_{min}(i)$ are illustrated in the top part of Figure 20. As can be seen, the interpolating functions represent the envelope of the signal $u(i)$. We now compute the average of the envelope $m(i) = (e_{max}(i) + e_{min}(i))/2$, which gives the local trend in the signal. Subtracting the local trend from the signal results in the local oscillation. Ideally, the local oscillation is a simple function with varying amplitude and frequency with zero mean value and with the number of extrema and the number of zero crossings differing by no more than one, called an intrinsic mode function (IMF). However in practice, these conditions do not immediately occur and a process of iteration called sifting is followed. The current local oscillation becomes the new signal for which new envelope functions are determined, labelled 'Sift 1' in Figure 20, and the average of the envelope is computed. This new local trend is subtracted from the current signal to obtain the new local oscillation. As noted in the figure, at least 8 siftings are required for the local trend to approach zero and the resulting IMF $C(i)$ to have zero mean. It should also be noted that the envelope of the IMF is approximately symmetric about the axis.

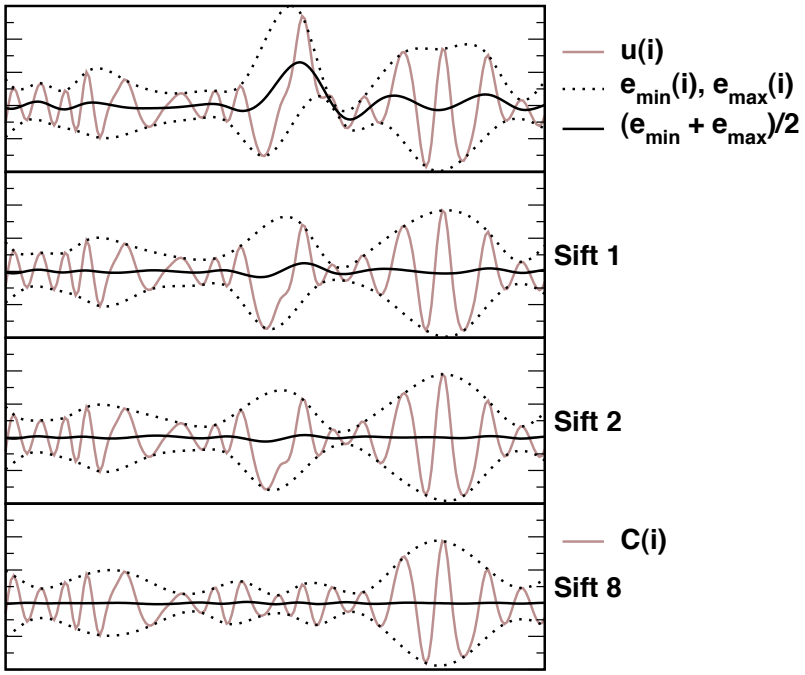

Figure 20. Example of the process of empirical mode decomposition.

Stopping Criteria

As stated in the main text, the criteria that a local oscillation must meet for it to be considered an IMF are:

1. The difference between the number of extrema and the number of zero crossings is at most one.
2. The average of the envelope along the signal is zero or near zero according to some convergence criterion.

To achieve these conditions in the numerical calculations, we followed the stopping criteria of Rilling et al.[18] First of all, the sifting will stop any time the number of extrema is less than or equal to 2. With sufficient extrema in the current local oscillation, we compute a relative mean amplitude at each data point.

$$s(i) = \left| \frac{e_{max}(i) + e_{min}(i)}{e_{max}(i) - e_{min}(i)} \right|$$

If the denominator is equal to zero, set $s(i) = 0$. To stop sifting, both the following must be true:

1. $s(i) < \phi_2$ at all points.
2. Let k be the number of points where $s(i) < \phi_1$, then $k/K \geq 1 - \alpha$. If $\alpha = 0.05$, then 95% of the points meet the condition $s(i) < \phi_1$.

To achieve these conditions, we must have $\phi_2 > \phi_1$. The recommended values of $\phi_2 = 0.5$ and $\phi_1 = 0.05$ given by Rilling et al.[18] were used.

Even though a stop-sifting criterion is specified, sifting can go on for many iterations potentially leading to undesirable results. Wu & Huang[19] discuss the issues involved with the inexactness of computing a stopping criterion and suggest setting the number of sifts to a fixed value of 10. We followed this by limiting the number of sifts to 10, but accepting less sifts if the above enumerated criteria were met.

Boundary Conditions

To obtain the envelopes of the signals shown on Figure 20, boundary values must be specified at the ends of the signal since typically these are not extreme points. We followed the procedure to extrapolate from the two extrema of the same type nearest the end point.[19] For the maxima envelope, if the extrapolated value is higher than the end point, choose the extrapolated value. Otherwise, keep the end point value. Similarly for the minima envelope, use the extrapolated value if it is lower than the end point value.

Appendix B – Statistics from the Ellipse Equation

The contours of a two-point, second-order correlation of the axial fluctuation velocity has an elliptic shape in the $(\eta_1/D, \tau U_J/D)$ plane, see Figure 8a for an example. To determine an equation for an ellipse, we extract coordinates for the points in the plane where the level is 1/e times the peak of the correlation using interpolation on the data grid. These points are fit to the ellipse equation

$$a\left(\frac{\eta_1}{D}\right)^2 + b\frac{\eta_1}{D}\frac{\tau U_J}{D} + c\left(\frac{\tau U_J}{D}\right)^2 + d\frac{\eta_1}{D} + e\frac{\tau U_J}{D} + f = 0 \tag{13}$$

using the least-squares, non-iterative approach from Halíř & Flusser[20] to obtain the coefficients a through f. Note from the diagram in Figure 21 that the center of the ellipse (x_c, y_c) does not necessarily coincide with the origin of the axis system.

Given the coefficients, we estimate the length scale as the distance from the origin to the ellipse along the line $\tau U_J/D = 0$. Substituting this into equation (13) and solving for η_1/D results in

$$\frac{L}{D} = -\left(\frac{d}{2a}\right) + \sqrt{\left(\frac{d}{2a}\right)^2 - \frac{f}{a}} \tag{14}$$

The time scale is found from the distance from the origin to the ellipse, where the semi-major axis a_x intersects the ellipse, and projected onto the $\tau U_J/D$ axis. Figure 21 shows this distance to be

$$\frac{\tau U_J}{D} = a_x \sin\alpha + y_c \tag{15}$$

The phase speed is determined from the angle of rotation the ellipse makes about the origin

$$\frac{U_c}{U_J} = \frac{1}{\tan\theta} \tag{16}$$

Using analytic geometry, equations are derived to aid in the solution of equations (15) and (16) based on the coefficients in equation (13).

$$\tan\theta = \frac{a_x \sin\alpha + y_c}{a_x \cos\alpha + x_c} \tag{17}$$

$$a_x = \sqrt{\frac{\mu\left(1 - \tan^2\alpha\right)}{a - c\tan^2\alpha}} \tag{18}$$

$$\mu = a\,x_c^2 + b\,x_c y_c + c\,y_c^2 - f \tag{19}$$

$$x_c = \frac{2\,c\,d - b\,e}{b^2 - 4\,a\,c} \tag{20}$$

$$y_c = \frac{2\,a\,e - b\,d}{b^2 - 4\,a\,c} \tag{21}$$

$$\tan\alpha = -\left(\frac{a-c}{b}\right) + \sqrt{\left(\frac{a-c}{b}\right)^2 + 1} \tag{22}$$

Acknowledgment

The author would like to thank Dr. Stewart J. Leib for many helpful discussions and Dr. James Bridges for providing the measured data and the software for computing correlations and spectra. The NASA Supersonics Project of the Fundamental Aeronautics Program supported this work.

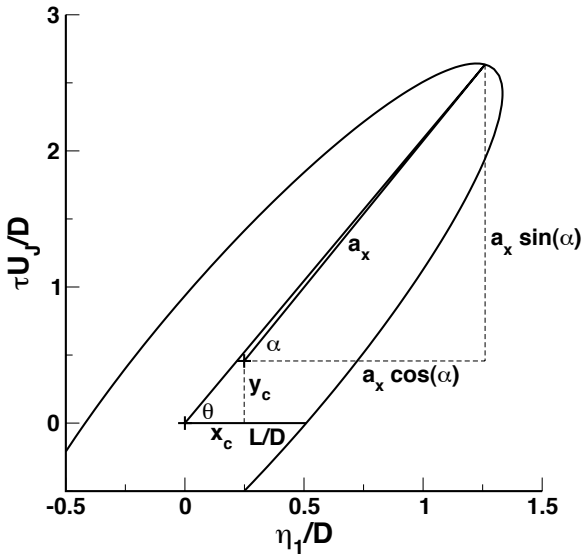

Figure 21. Diagram of ellipse system for computing phase velocity and length and time scales.

References

[1]Goldstein, M. E. and Leib, S. J., "The Aeroacoustics of Slowly Diverging Supersonic Jets," *J. Fluid Mech.*, Vol. 600, 2008, pp. 291–337.

[2]Bodony, D. J. and Lele, S. K., "A Statistical Subgrid Scale Noise Model: Formulation," AIAA Paper No. 2003-3252, 2003.

[3]Bodony, D. J. and Lele, S. K., "Spatial Scale Decomposition of Shear Layer Turbulence and the Sound Sources Associated with the Missing Scales in a Large-Eddy Simulation," AIAA Paper No. 2002-2454, 2002.

[4]Huang, N. E., Shen, Z., Long, S. R., Wu, M. C., Shih, H. H., Zheng, Q., Yen, N.-C., Tung, C. C., and Liu, H. H., "The Empirical Mode Decomposition and the Hilbert Spectrum for Nonlinear and Non-Stationary Time Series Analysis," *Proc. Roy. Soc. Lond. A*, Vol. 454, 1998, pp. 903–995.

[5]Huang, N. E., Shen, Z., and Long, S. R., "A New View of Nonlinear Water Waves: The Hilbert Spectrum," *Ann. Rev. Fluid Mech.*, Vol. 31, 1999, pp. 417–457.

[6]Huang, N. E. and Wu, Z., "A Review on Hilbert-Huang Transform: Method and its Applications to Geophysical Studies," *Rev. Geophys.*, Vol. 46, No. RG 2006, 2008.

[7]Bridges, J. and Brown, C. A., "Validation of the Small Hot Jet Acoustic Rig for Aeroacoustic Research," AIAA Paper No. 2005-2846, 2005.

[8]Wernet, M. P., "Temporally Resolved PIV for Space-Time Correlations in Both Cold and Hot Jet Flows," *Measurement Science and Technology*, Vol. 18, 2007, pp. 1387–1403.

[9]Bridges, J. and Wernet, M. P., "Effect of Temperature on Jet Velocity Spectra," AIAA Paper No. 2007-3628, 2007.

[10]Flandrin, P., Rilling, G., and Gonçalvés, P., "Empirical Mode Decomposition as a Filter Bank," *IEEE Sig. Proc. Let.*, Vol. 11, No. 2, 2004, pp. 112–114.

[11]Wu, Z. and Huang, N. E., "A Study of the Characteristics of White Noise using the Empirical Mode Decomposition Method," *Proc. Roy. Soc. Lond. A*, Vol. 460, 2004, pp. 1597–1611.

[12]Huang, Y., Schmitt, F. G., Lu, Z., and Liu, Y., "Empirical Mode Decomposition Analysis of Experimental Homogeneous Turbulence Time Series," Colloque GRETSI 11–14 September, Troyes, France, 2007.

[13]Kerhervé, F., Fitzpatrick, J., and Jordan, P., "The Frequency Dependence of Jet Turbulence for Noise Source Modelling," *J. Sound Vib.*, Vol. 296, 2006, pp. 209–225.

[14]Morris, P. J. and Zaman, K. B. M. Q., "Velocity Measurements in Jets with Application to Noise Source Modeling," *J. Sound Vib.*, Vol. 329, 2010, pp. 394–414.

[15]Bendat, J. S. and Piersol, A. G., *Random Data Analysis and Measurement Procedures*, Wiley-Interscience, New York, NY, 2nd ed., 1986.

[16]Rabiner, L. R., Schafer, R. W., and Dlugos, D., "Periodogram Method for Power Spectrum Estimation," *Programs for Digital Signal Processing*, Section 2.1, IEEE Press, 1979, pp. 2.1–1–2.1–10.

[17]Harper-Bourne, M., "Jet Noise Turbulence Measurements," AIAA Paper No. 2003-3214, 2003.

[18]Rilling, G., Flandrin, P., and Gonçalvés, P., "On Empirical Mode Decomposition and its Algorithms," *IEEE-EURASIP Workshop on Nonlinear Signal and Image Processing*, No. NSIP-03 Grado(I), June 2003.

[19]Wu, Z. and Huang, N. E., "Ensemble Empirical Mode Decomposition: A Noise-Assisted Data Analysis Method," *Adv. Adapt. Data Anal.*, Vol. 1, No. 1, 2009, pp. 1–41.

[20]Halíř, R. and Flusser, J., "Numerically Stable Direct Least Squares Fitting of Ellipses," *Proc. 6th Int. Conf. in Central Europe on Computer Graphics, Visualization and Interactive Digital Media WSCG*, 1998, pp. 125–132.